Available online at www.sciencedirect.com

SciVerse ScienceDirect

Ceramics International 39 (2013) 4329–4337

CERAMICS INTERNATIONAL

www.elsevier.com/locate/ceramint

Synthesis and characterization of fluorapatite–zirconia composite nanopowders

Bahman Nasiri-Tabrizi*, Abbas Fahami

Materials Engineering Department, Najafabad Branch, Islamic Azad University, Najafabad, Isfahan, Iran

Received 16 October 2012; received in revised form 7 November 2012; accepted 8 November 2012
Available online 14 November 2012

Abstract

The structural and morphological features of fluorapatite–zirconia composite nanopowders during mechanochemical process and subsequent thermal treatment were investigated. The experimental outcomes were characterized by X-ray diffraction (XRD), Fourier transform infrared spectroscopy (FT-IR), energy dispersive X-ray spectroscopy (EDX), and field emission scanning electron microscopy (FE-SEM). After 300 min of milling, the average crystallite size, lattice strain, and the volume fraction of grain boundaries of fluorapatite were about 29 nm, 0.543%, and 9.64%, respectively. According to morphological evaluation, a fine homogeneous microstructure was obtained after 300 min of milling. The annealed sample at 600 °C exhibited grain size of about 32 nm for fluorapatite and 37 nm for monoclinic zirconia. During heating at 900 °C, fluorapatite decomposed to tricalcium phosphate (β-TCP) and calcium fluoride. With increase of temperature from 600 to 900 °C, the crystallite size of fluorapatite and monoclinic zirconia reached 43 and 40 nm, respectively. According to the FE-SEM micrographs, heat treated samples were composed of particles with a mean particle size of about 33 nm at 600 °C and 209 nm at 900 °C.

Keywords: Mechanochemical; Fluorapatite; Composite materials; Structural features

1. Introduction

Bioceramics are an important subset of biomaterials which became an accepted group of materials for medical applications, mainly for implants in orthopedics, maxillofacial surgery and dental implants. Among them, hydroxyapatite (HAp, $Ca_{10}(PO4)_6(OH)_2$) seems to be the most appropriate ceramic material for artificial bone and tooth applications owing to its excellent biocompatibility and bioactivity [1]. However, HAp has intrinsically high dissolution rate in a biological system, poor corrosion resistance in an acidic environment, and poor chemical stability at high temperature [2,3]. It has been found that, the biological and physicochemical properties of HAp can be improved by being substituted with ions that usually exist in natural apatites of bone [4]. In fact, trace ions substituted in apatites can affect the lattice parameters, crystallinity, dissolution kinetics and other physical properties [5]. If OH^- groups in HAp are partially replaced by F^-, fluoride-substituted HAp (FHAp, $Ca_{10}(PO_4)_6(OH)_{2-x}F_x$) is obtained. When the substitution is complete, fluorapatite (FAp, $Ca_{10}(PO_4)_6F_2$) is formed. When fluoride consumed in optimal amounts in water and food, used topically in toothpaste and mouth rinses, it increases tooth mineralization and bone density, reduces the risk and prevalence of dental caries, and promotes enamel remineralization throughout life for individuals of all ages [6]. Moreover, the incorporation of fluorine into HAp induces better biological response [7].

On the other hand, the incorporation of bioinert ceramics into calcium phosphate-based materials has shown significant improvement in structural features as well as mechanical properties. Therefore, many attempts have been made to improve the functional characteristics of bioceramics through the incorporation of ceramic second phases [8–11]. An ideal reinforcing material for the calcium phosphate-based composites, which satisfies all requirements, has not yet been found. However, some attempts have been made to develop HAp- and FHAp-based composites such as HAp–Al_2O_3 [8], HAp–ZrO_2 [12], HAp–TiO_2 [13], FHAp–Al_2O_3 [14], and

*Corresponding author. Tel.: +98 3114456551; fax: +98 3312291008.
E-mail address: bahman_nasiri@hotmail.com (B. Nasiri-Tabrizi).

0272-8842/$ - see front matter © 2012 Elsevier Ltd and Techna Group S.r.l. All rights reserved.
http://dx.doi.org/10.1016/j.ceramint.2012.11.016

FHAp–ZrO_2 [15] composites. These studies indicate that two major common phenomena ordinarily happen that comprise dissociation of HAp to tricalcium phosphate (α/β-TCP) and interfacial reactions between HAp and reinforcement ceramic phase, which can lead to the formation of $CaZrO_3$ and $CaTiO_3$. Among the second phases, ZrO_2 has been studied extensively because of its relatively higher mechanical strength and toughness [9,10,12]. However, the addition of ZrO_2 results in lowering the decomposition temperature of microcrystalline HAp- and FHAp-based composites below the sintering temperature which causes an adverse influence on the mechanical properties [15]. These events are related to the structural features of composite that are affected by the synthesis process. Generally, in order to prepare calcium phosphate-based composites, calcium phosphate source chemicals and ZrO_2 powders are mixed, cold pressed and then sintered at high temperatures [9]. Under these circumstances, the products have microcrystalline structure. Since the nanocrystalline structures, compared to the microcrystalline structures, are more important to achieve high thermal stability and mechanical properties [16], the FAp–ZrO_2 composites with nanostructural characteristics are designated for medical applications. Hence, synthesis and characterization of FAp–ZrO_2 composite nanopowders via one-step mechanochemical process and subsequent thermal treatment provided the main target for current investigation. A review of scientific research shows that the mechanochemical process has a lot of well-known inherent advantages because of being both economically and technically a simple approach mass production, and the marvelous flexibility to generate nanostructured bioceramics [17,18]. In the field of nanocomposites, this technique can lead to the formation of interpenetrating phase composites with nano-sized structures. These structures exhibit properties and performance which are much more improved over their conventional microcrystalline counterparts [16–18].

Despite the fact that FAp-based materials are known to have greater thermal and chemical stability than those of HAp [3], only a limited number of studies have been conducted on the production of FAp-based nanocomposites [10,19]. Consequently, the aim of this study was to examine the structural features (crystallite size, lattice strain, volume fraction of grain boundary, and crystallinity) and morphological characteristics (particle size and shape, particle distribution and agglomeration) of novel FAp-based composite nanopowders during mechanochemical process and subsequent thermal treatment. In fact, the effects of milling time and succeeding heat treatment have been explored with the purpose of recommending a proper circumstance for the mass production of FAp–ZrO_2 composite nanopowders.

2. Materials and methods

2.1. Synthesis of nanopowders

The FAp–ZrO_2 composite nanopowders were prepared by mechanochemical process using calcium oxide (CaO, Merck), phosphorous pentoxide (P_2O_5, Merck), calcium fluoride (CaF_2,Merck), and monoclinic zirconia (*m*-ZrO_2, Merck) as starting reagents. The mechanochemical synthesis was performed in a planetary ball mill at 600 rpm. Zirconia balls (20 mm in diameter) were used in sealed cylindrical polyamide—6 vials (vol. 125 ml). The weight ratio of ball-to-powder was 20:1. Ball milling of powder mixture was carried out at room temperature under ambient air atmosphere without using any process control agent (PCA). In order to avoid excessive temperature rise within the grinding vial, 45 min ball milling duration was followed by an interval of 15 min. To synthesize FAp–5 wt% ZrO_2 composite nanopowders the distinct amount of *m*-ZrO_2 (5 wt%) was mixed with CaO, P_2O_5, and CaF_2 according to Reaction (1), and then they were milled in planetary ball mill for 5, 15, 30, and 300 min.

$$9CaO + 3P_2O_5 + CaF_2 + m\text{-}ZrO_2 \rightarrow Ca_{10}(PO_4)_6F_2 + m\text{-}ZrO_2 \quad (1)$$

After that the resultant powders were filled in a quartz boat, and then annealed for 1 h under atmospheric pressure at 600 and 900 °C. The heating rate from room temperature up to the desired temperature was fixed at 10 °C min^{-1}.

2.2. Characterization of nanopowders

Phase analyses and structural changes of composite powders were determined by X-ray diffraction (Philips X-ray diffractometer (XRD), *Cu-*K_α radiation, 40 kV, 30 mA and 0.02° s^{-1} step scan). For qualitative analysis, XRD graphs were recorded in the interval $20° \le 2\theta \le 60°$ at scan speed of 1°/min. "*PANalytical X'Pert HighScore*" software was also utilized for the analysis of different peaks. The gained patterns were compared to standards compiled by the Joint Committee on Powder Diffraction and Standards (JCPDS), which involved card #15-0876 for FAp, #037-1497 for CaO, #035-0816 for CaF_2, #01-1079 for $Ca(OH)_2$, #05-0318 for P_2O_5, and #037-1484 for *m*-ZrO_2. Crystallite size and lattice strain of the samples were determined by using the XRD data according to the following equations [19]:

$$D = \frac{K\lambda}{(b_{obs} - b_{std})(b\cos\theta)} \quad (I)$$

$$E^2 = \frac{\left(b_{obs}{}^2 - b_{std}{}^2\right)}{(4\tan\theta)^2} \quad (II)$$

where b (in radians) is the structural broadening, which is the difference in integral profile width between a standard and the unknown sample and K, λ, D, E, and θ are the shape coefficient (value between 0.9 and 1.0), the wavelength of the X-ray used (0.154056 nm), crystallite size, lattice strain and the Bragg angle (°), respectively.

If we assume that a crystallite is a sphere of diameter D surrounded by a shell of grain boundary with thickness t,

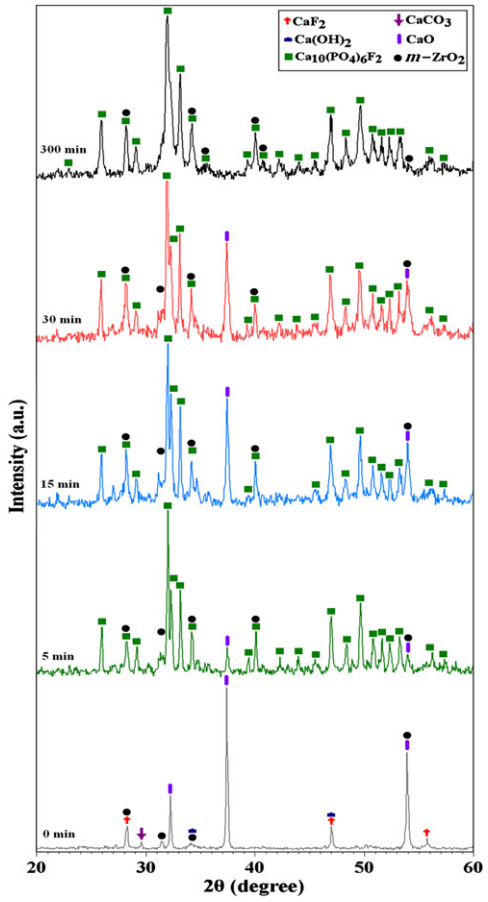

Fig. 1. XRD patterns of powder mixture before and after one step mechanochemical process for 5–300 min.

the volume fraction of grain boundary, f, is approximately [20]

$$f = 1 - \left[\frac{D}{(D+t)}\right]^3 \quad \text{(III)}$$

Values of f were calculated from this equation by substituting the experimental crystallite size obtained by XRD with D under the assumption of $t = 1$ nm.

On the other hand, the relation between lattice spacing (d) and lattice parameters (a, b, and c) of the hexagonal structures (FAp in the composite) is shown as [21]:

$$\frac{1}{d^2} = \frac{4}{3}\frac{h^2+hk+k^2}{a^2} + \frac{l^2}{c^2} \quad \text{(IV)}$$

where h, k, l are the Miller indices of the reflection planes. The (002) and (300) reflections were chosen for the lattice parameters calculation.

Meanwhile, volume V of the hexagonal unit cell was determined by the following formula [12]:

$$V = 2.589a^2c \quad \text{(V)}$$

In addition, the crystallinity of FAp after thermal annealing process was determined from the XRD data using the following equation [22]:

$$Xc = 1 - \left(\frac{V_{112/300}}{I_{300}}\right) \quad \text{(VI)}$$

where X_c is the degree of FAp crystallinity, I_{300} is the intensity of the (300) peak, and $V_{112/300}$ is the intensity of the shoulder between the (112) and (300) diffraction peaks.

Fourier transform infrared (FT-IR, Model 680 Plus, JASCO) spectroscopy was also utilized to characterize the products. 1 mg of the powdered sample was mixed with 200 mg spectroscopic grade KBr by hand milling the powder in an agate mortar. Subsequently, the transmittance spectroscopy was recorded in the range 4000–400 cm^{-1} at 2 cm^{-1} resolution by 16 scans. Energy dispersive X-ray spectroscopy (EDX) which was coupled with SEM (SERON AIS–2100) was used for semi-quantitative examination of the samples (voltage used for EDX was equal to 20 kV). The size and morphology of fine powders and agglomerates were observed on a field emission scanning electron microscope (FE-SEM Hitachi S1831) that operated at the acceleration voltage of 15 kV. Prior to FE-SEM analysis, the milled powders were suspended in ethanol and dispersed ultrasonically for 3 min. In the next step, the powder samples were coated with gold for more electronic conduction.

3. Results and discussion

3.1. XRD analysis

3.1.1. Phase determination

Fig. 1 shows the XRD patterns of CaO, P_2O_5, and CaF_2 powder mixture in the presence of 5 wt% m-ZrO_2 before and after mechanical activation for different milling times. According to the XRD patterns, it can be seen that after 5 min of milling the phase compositions were FAp and m-ZrO_2 with a trace of CaO. After 15 and 30 min of milling, similar to previous sample, the main product of mechanochemical reaction was FAp–ZrO_2 composite with a small amount of CaO. This suggests that CaO was still present in the samples after 5, 15, and 30 min of milling. When the mechanical activation time was extended to 300 min, all the peaks corresponding to CaO had vanished and only those belonging to FAp and m-ZrO_2 were visible. According to Fig. 1, it could be noted that the intensity decreasing rate of each starting material differed. By comparing the relative intensity peaks of CaF_2 and CaO during milling, it was found that the peak intensity of CaO decreased relatively slowly, while CaF_2 completely vanished after 5 min of milling. Eventually, FAp–5 wt% ZrO_2 composite with no impurity phase was formed after 300 min of milling.

3.1.2. Structural features

Fig. 2 displays the effect of milling time on the average crystallite size, volume fraction of grain boundaries, and lattice strain of FAp in the composite structures which were calculated using XRD data. According to this figure, the crystallite size of the specimens decreased with

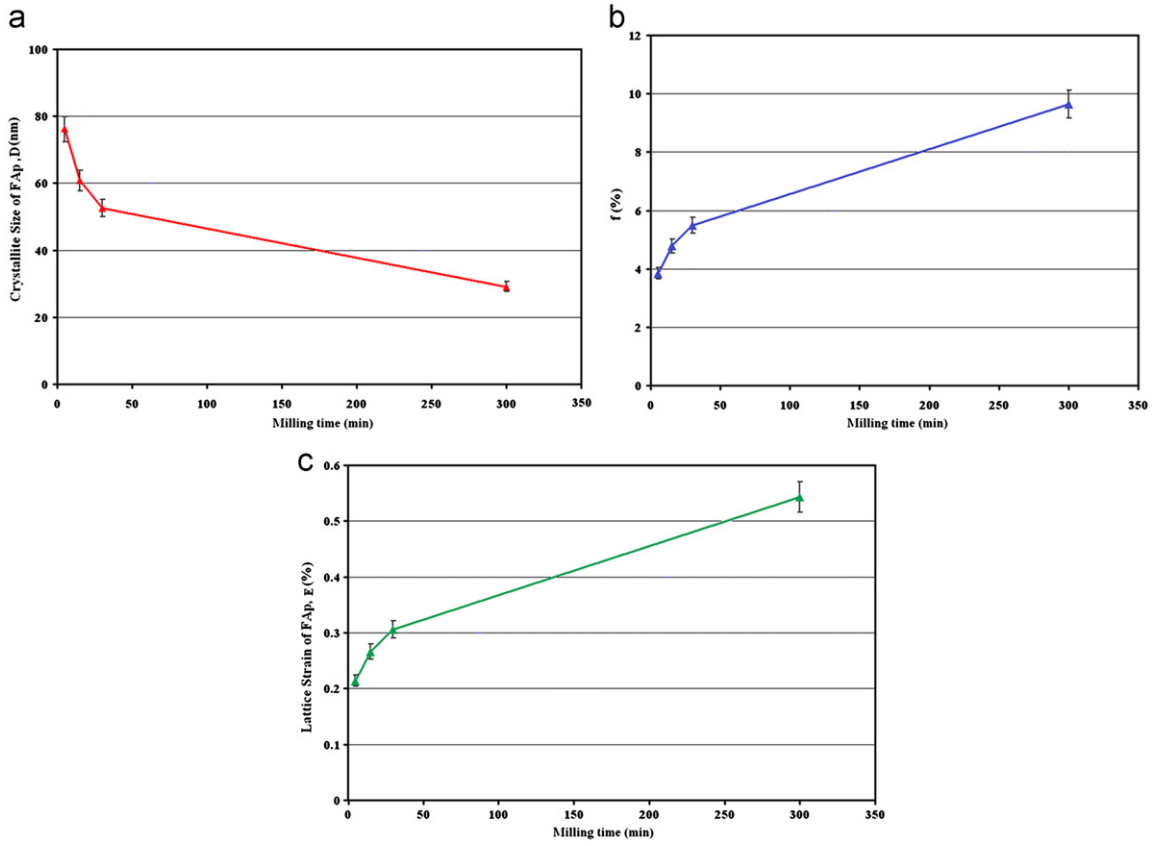

Fig. 2. (a) Average crystallite size, (b) the volume fraction of grain boundaries, and (c) lattice strain of FAp in the composite structures as a function of milling time.

increasing milling time. Conversely, the lattice strain and volume fraction of grain boundaries increased with increasing milling time. This phenomenon was attributed to the effect of mechanical activation on the structural features. Finally, crystallite size, lattice strain, and the volume fraction of grain boundaries of FAp after 300 min of milling were about 29 nm, 0.543%, and 9.64%, respectively. The obtained data show that by increasing the milling time from 5 min to 300 min, the crystallite size decreases mostly after 30 min and reaches a minimum at 300 min of milling time. It seems that the presence of m-ZrO_2 as second phase particles changes the local dislocation density distribution, owing to strain incompatibility between the matrix and particles which may cause excessive accumulation of internal strain. This reveals the effectiveness of added second phase particles in accelerating grain size reduction. This result is in agreement with other references [12]. It should be noted that the average crystallite size of the m-ZrO_2 was about 26 nm after 300 min of milling.

Comparable graphs of a-−axis, c-axis, and the unit cell volume changes of the samples as a function of milling time are shown in Fig. 3a–c. As can be seen in Fig. 3, the a-axis values for FAp were similar to the reported values for standard FAp (♯15-0876: a=9.368 Å). Similarly, there were little changes in the c-axis values (FAp ♯15-0876: c=6.884 Å). On the other hand, the determined amounts of unit cell volume of FAp demonstrate that by choosing the total milling time to 300 min, the unit cell volume increases first and reaches a maximum at 30 min of milling, and then by further increasing the milling time to 300 min, the unit cell volume decreases. These variations in cell volume resulted mainly from increases in the a parameters, rather than from the c values and can probably be attributed to the lattice distortion of FAp during milling of the samples. The similarity of the values obtained in this paper to standard values provides further support for the purity of the samples that have been produced by the mechanochemical process.

3.2. FT-IR evaluation

FT-IR spectra of the samples milled for various periods of time are shown in Fig. 4. These spectra reflect the presence of functional groups that determine the composition of the samples and the changes that occurred during the mechanochemical process. In the FT-IR spectra of the samples, two bands relating to the vibration of the adsorbed water in the apatite structure were detected [23]. For the samples which were milled in the range of 15–300 min, a doublet appears at 1429 and 1457 cm^{-1} corresponding to v_3 and a band at 865 cm^{-1} corresponding to v_2 vibration mode of the carbonated groups which showed that FAp contained some CO_3^{2-} groups in PO_4^{3-}

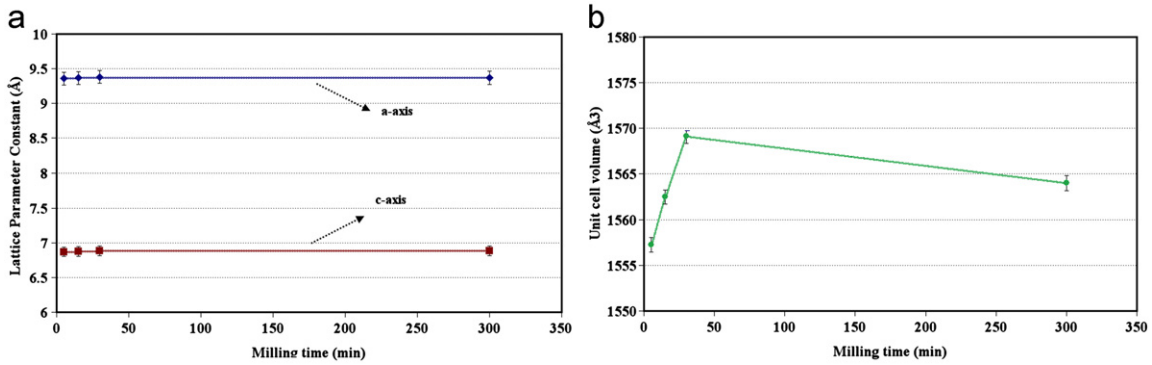

Fig. 3. (a) Change in the lattice constants and (b) their unit cell volume for FAp in the composite structures as a function of milling time.

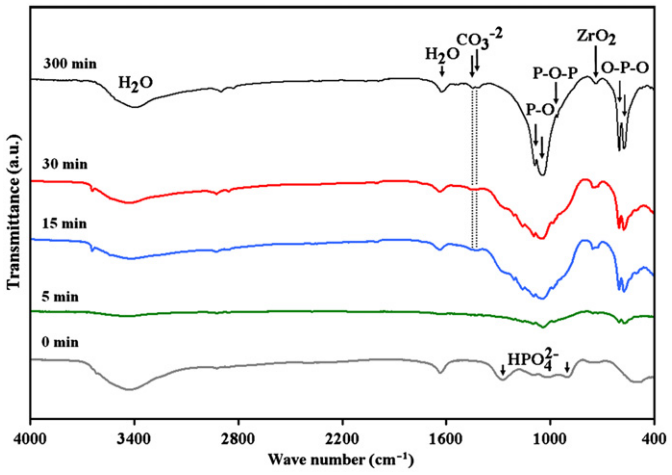

Fig. 4. FT-IR spectra of the samples before and after one step mechanochemical process for 5–300 min.

sites of apatite lattice (B-type substitution) [24]. It has been reported that this kind of apatite is more similar to biological apatite and could be more suitable for bone replacement materials [23]. It should be noted that the FT-IR band at 1429 and 1457 cm^{-1} corresponding to v_3 and a band at 865 cm^{-1} corresponding to v_2 vibration mode of the carbonated groups together with the structural changes in FAp (calculated from XRD data) supports the existence of carbonated groups. The main characteristic peaks of PO_4^{3-} group which had four distinct asymmetrical stretching vibration modes, namely v_1 (P–O–P), v_2 (P–O–P), v_3 (P–O), and v_4 (O–P–O) were clearly observed, given as follows. The v_1 and v_2 vibration peaks were observed at 965 and 473 cm^{-1}, respectively. The v_3 vibration peak was noted in the region between 1094 and 1049 cm^{-1}, which was the most intensified peak among the phosphate vibration modes. The band between 603 and 575 cm^{-1} showed v_4 vibration mode of PO_4^{3-} group. Comparison between FT-IR spectra of the milled samples and the spectrum of the starting mixture confirmed a substantial change in the system phase composition, which happened during the mechanochemical process. The bands at 900 and 1273 cm^{-1} were assigned to the HPO_4^{2-} group vibrations [23], which slowly diminished with increase of milling time and finally disappeared after 300 min of milling. For the sample which was milled for 300 min, the band at 965 cm^{-1} corresponds to v_1 vibration of the PO_4^{3-} group. This band appeared as a result of HPO_4^{2-} group depredation. According to literature [11], the band at 741 cm^{-1} corresponds to the vibration of ZrO_2 with a small differences depending upon the milling time. It should be noted that the intermediate peak at approximately 2929 cm^{-1} is not the characteristic of the samples; this belongs to KBr itself [13]. The result of FT-IR spectra revealed that the resultant powders have an appropriate purity.

3.3. Morphological characteristics and EDX analysis

The performance of nanobioceramics in biomedical applications is effectively dependent on their morphological features [1]. However, particle shape analysis is one of the most difficult problems in powder technology as there is no general shape factor available that clearly differentiates all possible kinds of morphologies [25]. For a better understanding of the effect of mechanochemical process on the morphological features, FE-SEM analysis was performed on the composite nanopowders. Fig. 5 shows the morphology and particle size distribution of the composite powders milled from 5 min to 300 min. In general, deformation, fracture and cold welding of powders occur in the early stages of milling [17]. After 5 min of milling, some large platelet agglomerates/particles were formed because they may undergo different compression and wear forces of the colliding balls (Fig. 5a and b). According to Fig. 5a and b, a considerable activation occurred in the powder mixture after 5 min of milling. Since, the XRD analysis confirmed the formation of FAp–5 wt% *m*-ZrO_2 composite nanopowder after 5 min of milling, we concluded that the localized heating and pressure at regions of contact between the reactant with fine grains may be an important factor for the phase formation in the activated sample for 5 min of milling. With increasing milling time up to 30 min, all the platelet particles were fractured into smaller particle sizes (Fig. 5c and d). By increasing milling

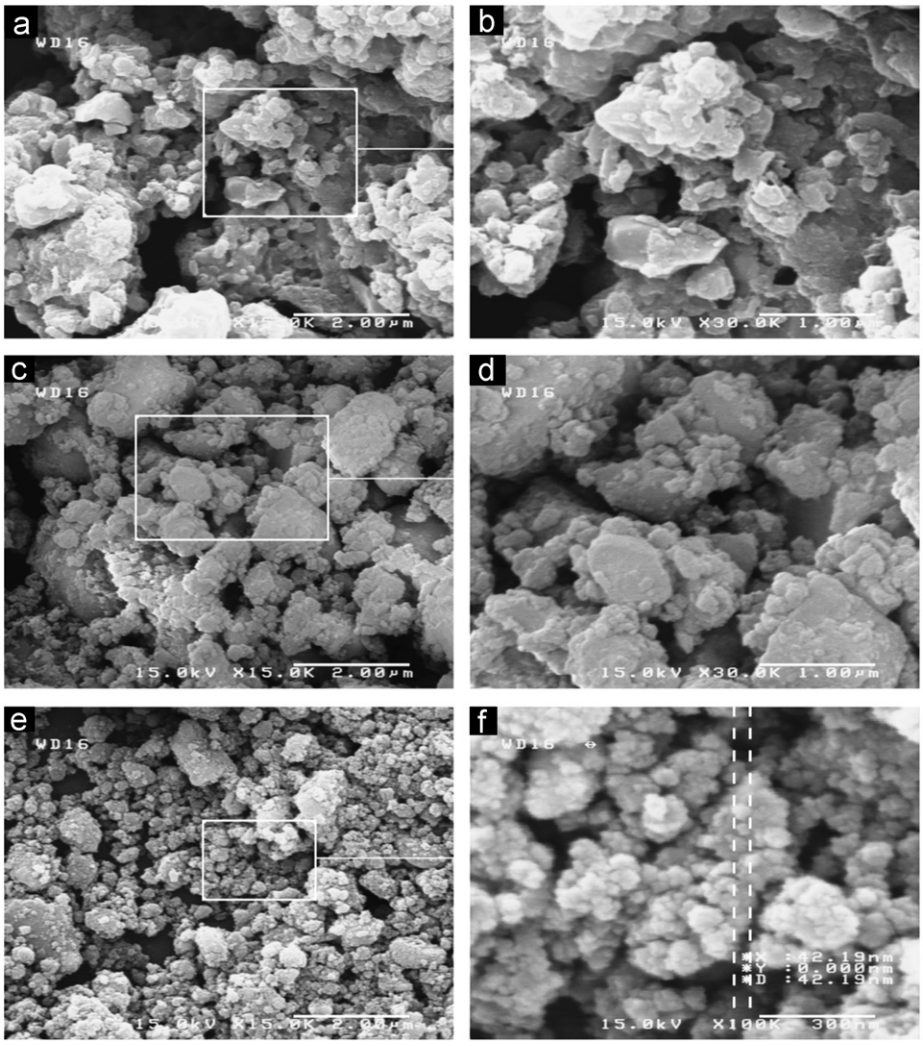

Fig. 5. FE-SEM images of the composite nanopowders after different milling times: (a,b) 5 min, (c,d) 30 min, and (e,f) 300 min.

time to 300 min, the rate of fracturing increased and as a result the size of powder particles decreased. At this stage, the morphology of powder nanoparticles was almost equiaxed with the average size of about 45 nm (Fig. 5e and f). Based on FE-SEM images, in comparison with other samples, the product after 300 min of milling has a fine homogeneous microstructure.

Fig. 6 shows the EDX spectra of the samples after 5 and 300 min of milling, indicating that the Ca, P, O, F, and Zr exist inside the particles. The EDX results confirmed that a very homogeneous distribution of components was formed during one-step mechanochemical process particularly after 300 min of milling. In accordance with EDX point chemical analysis, it was identified that no chemically stable contaminants were detected due to the excessive adhesion of powders to the milling media. It should be mentioned that the use of polymeric vial has been proposed in the authors' experiments not only to annihilate contamination problem, but also to achieve modified morphologies with high biomedical performance [26–29].

3.4. Thermal treatment

To examine the effect of thermal treatment on the phase transformations and structural features, heat treatment was carried out on FAp–ZrO_2 composite nanopowders at 600 and 900 °C for 1 h. Fig. 7 shows the XRD patterns of the composite nanopowders after thermal annealing process. As can be seen in Fig. 7, annealing at 900 °C led to the decomposition of FAp to $Ca_3(PO_4)_2$ and CaF_2. Hence, the following reaction was proposed:

$$Ca_{10}(PO_4)_6F_2 \rightarrow 3Ca_3(PO_4)_2 + CaF_2 \quad (2)$$

At the lower heat treatment temperature (600 °C), the poor crystalline apatite phase was characterized by broad diffraction bands. In addition to the poor crystalline phase of FAp, the phase of *m*-ZrO_2 was also observed in this sample. With increase of temperature from 600 to 900 °C, the existence of FAp and *m*-ZrO_2 phases together with minor β-TCP phase was verified. This suggests that the partial decomposition of FAp occurs even at 900 °C in the

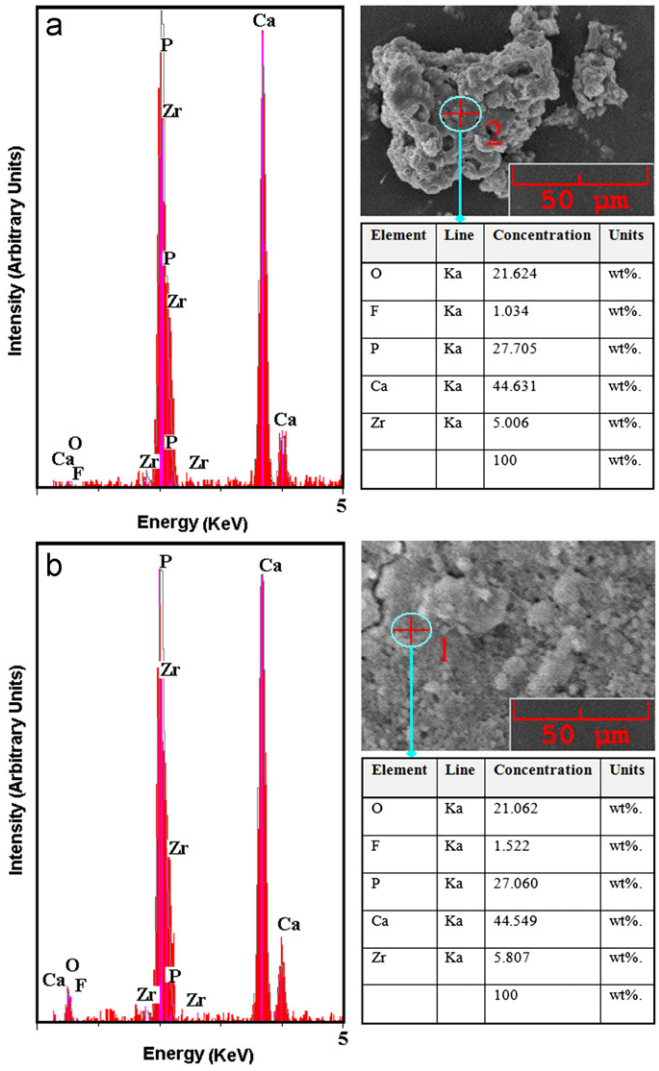

Element	Line	Concentration	Units
O	Ka	21.624	wt%.
F	Ka	1.034	wt%.
P	Ka	27.705	wt%.
Ca	Ka	44.631	wt%.
Zr	Ka	5.006	wt%.
		100	wt%.

Element	Line	Concentration	Units
O	Ka	21.062	wt%.
F	Ka	1.522	wt%.
P	Ka	27.060	wt%.
Ca	Ka	44.549	wt%.
Zr	Ka	5.807	wt%.
		100	wt%.

Fig. 6. EDX spectra of the composite nanopowders after different milling times: (a) 5 min and (b) 300 min of milling.

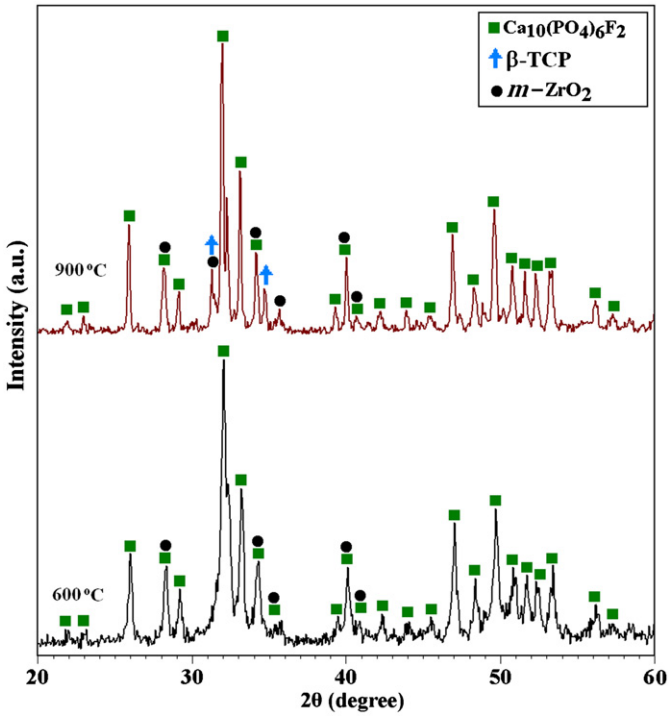

Fig. 7. XRD patterns of the composite nanopowders after thermal annealing process in the range of 600–900 °C for 1 h.

Table 1
Calculated lattice parameters of FAp in FAp–ZrO_2 composite nanopowders after thermal annealing process.

Sample	Corresponding phase	*a*-axis (Å)	*c*-axis (Å)	Unit cell volume (Å^3)
Milling (300 min)+600 °C	FAp	9.383	6.859	1563.377
Milling (300 min)+900 °C	FAp	9.375	6.884	1566.528
JCPDS #15-0876	FAp	9.368	6.884	1564.264

presence of zirconia. It has been reported [13,29] that the final microstructure of TCP will contain β or α-TCP depending on their cooling rate. Rapid cooling from sintering temperature gives rise to α-TCP phase only, whereas slow furnace cooling leads to β-TCP phase only. Any moderate cooling rate between these two results in mixed phases of both β and α-TCP. Thus, in the present investigation the slow furnace cooling rate leads to formation of β-TCP phase in heat treated samples.

Based on the calculated data from the XRD profiles, the sample annealed at 600 °C showed small grains of about 32 and 37 nm for FAp and *m*-ZrO_2, respectively. With increase of temperature from 600 to 900 °C, grain growth happened so that the crystallite size of FAp and *m*-ZrO_2 reached 43 and 40 nm, respectively. Therefore, increasing the annealing temperature might assist grain growth although all the composite powders were comprised of nano-size crystallites. A similar trend was observed in the crystallinity as well as in the crystallite size, that is, an increase in the crystallinity from 14% up to the 71% with increasing heat treatment temperature from 600 °C to 900 °C.

The changes in lattice constants and the unit cell volume for FAp in the heat treated composites are summarized in Table 1. As can be seen, the volume of FAp unit cell increased after annealing between 600 and 900 °C. These increases in volume resulted mainly from increases in the *a* parameters, rather than from the *c* values. According to Reaction (2), the removal of calcium ions from FAp involves an ion exchange reaction with ZrO^{2+} ions from the *m*-ZrO_2 which can occur where the surfaces of *m*-ZrO_2 and FAp are in contact, with minimum rearrangement of their structures. The radius of a ZrO^{2+} ion is about 0.21 nm and that of calcium is about 0.1 nm [12]. This exchange, therefore, explains the increased volume of the FAp unit cell as shown in Table 1. In addition, the large ZrO^{2+} ion introduces strain into the FAp structure, accelerating the FAp decomposition process.

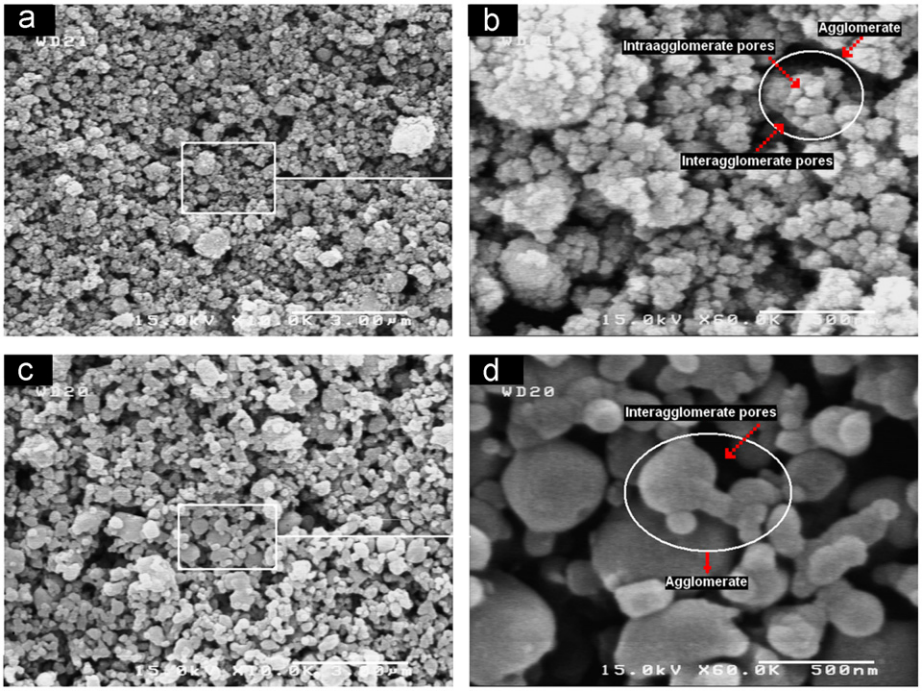

Fig. 8. FE-SEM images of FAp–ZrO_2 composite nanopowders annealed at (a,b) 600 and (c,d) 900 °C.

Fig. 6 shows the morphological features of FAp–ZrO_2 composite nanopowders annealed in the range of 600–900 °C. These observations clearly reveal a distinct difference in the samples' microstructure. At 600 °C (Fig. 8a and b), the product was composed of both agglomerates and fine particles. A higher magnification of FE-SEM image indicates that each agglomerate consists of many smaller particles having a size of about 33 nm (Fig. 8b). According to this figure, the intra-agglomerate pore sizes were much smaller than the interagglomerate pore sizes; thus, during the annealing process at ≥ 600 °C, the smaller intra-agglomerate pores were removed at a much faster rate than the larger interagglomerate pores due to higher driving force for annihilation. With increasing annealing temperature from 600 °C to 900 °C the powder particles became nearly equiaxed in shape with a mean grain size of about 209 nm (Fig. 8c and d). Meanwhile, the number of intra-agglomerate pores was much smaller than that in the powder heat treated at 600 °C (Fig. 8d). According to the FE-SEM observations, the increase in average size of resultant agglomerate with increase of heat treatment temperature can be attributed to the coalescence of agglomerates.

Generally, spherical geometry is better than other irregular shapes for achieving osseointegration because of the well space fillings and the low percentage of voids in the final product [26]. In addition, small content of β-TCP in apatite phases would be helpful for the strong and fast bonding to the natural bones by rapid resorption [30]. Therefore, the obtained products after annealing at temperature in the range of 600–900 °C are preferred in medical applications.

It should be mentioned that higher sintering temperature (≥ 900 °C) leads to enhanced grain growth, which changes morphological features of the composites.

4. Conclusions

Novel fluorapatite-based composite nanopowders were synthesized via mechanochemical process and subsequent thermal treatment. The effects of mechanical activation and thermal treatment on the structural and morphological features of the experimental outcomes were discussed. XRD patterns confirmed that the FAp–5 wt% ZrO_2 composite nanopowders were successfully produced after 5 min of milling. However, ball milling up to 300 min resulted in FAp–ZrO_2 composite nanopowders with no impurity phase. The determined amounts of structural features illustrated that by increasing the milling time from 5 min to 300 min, the crystallite size decreased mostly after 30 min and reached a minimum at 300 min of milling time. According to FE-SEM observations, the product after 300 min of milling has a fine homogeneous microstructure with the average particle size of about 45 nm. Thermal treatment at 900 °C led to the decomposition of FAp to $Ca_3(PO_4)_2$ and CaF_2. With increase of annealing temperature from 600 to 900 °C, grain growth occurred and as a result the crystallite size and crystallinity of FAp reached 43 nm and 71%, respectively. In accordance with FE-SEM images, at 600 °C the product was composed of both agglomerates and fine particles ($\sim$33 nm). After annealing at 900 °C the powder particles became nearly equiaxed in shape with a mean grain size of about 209 nm.

Acknowledgment

The authors are grateful to Research Affairs of Islamic Azad University, Najafabad Branch, for supporting of this research.

References

[1] S.J. Kalita, A. Bhardwaj, H.A. Bhatt, Nanocrystalline calcium phosphate ceramics in biomedical engineering, Materials Science and Engineering C 27 (2007) 441–449.
[2] M. Fini, L. Savarino, N.N. Aldini, L. Martini, G. Giavaresi, G. Rizzi, D. Martini, A. Ruggeri, A. Giunti, R. Giardino, Biomechanical and histomorphometric investigations on two morphologically differing titanium surfaces with and without fluorohydroxyapatite coating: an experimental study in sheep tibiae, Biomaterials 24 (2003) 3183–3192.
[3] Y. Chen, X. Miao, Thermal and chemical stability of fluorohydroxyapatite ceramics with different fluorine contents, Biomaterials 26 (2005) 1205–1210.
[4] E. Jallot, J.M. Nedelec, A.S. Grimault, E. Chassot, A. Grandjean-Laquerriere, P. Laquerriere, D. Laurent-Maquin, STEM and EDXS characterisation of physico-chemical reactions at the periphery of sol–gel derived Zn-substituted hydroxyapatites during interactions with biological fluids, Colloids and Surfaces B: Biointerfaces 42 (2005) 205–210.
[5] I. Mayera, J.D.B. Featherstone, Dissolution studies of Zn-containing carbonated hydroxyapatites, Journal of Crystal Growth 219 (2000) 98–101.
[6] C.A. Palmer, J.J.B. Anderson, Position of the American dietetic association:the impact of fluoride on health, Journal of the American Dietetic Association 101 (2001) 126–132.
[7] N. Rameshbabu, T.S. Sampath Kumar, K. Prasad Rao, Synthesis of nanocrystalline fluorinated hydroxyapatite by microwave processing and its in vitro dissolution study, Bulletin of Materials Science 29 (2006) 611–615.
[8] B. Viswanath, N. Ravishankar, Interfacial reactions in hydroxyapatite/alumina nanocomposites, Scripta Materialia 55 (2006) 863–866.
[9] R.R. Rao, T.S. Kannan, Synthesis and sintering of hydroxyapatite–zirconia composites, Materials Science and Engineering C 20 (2002) 187–193.
[10] F. Ben Ayed, J. Bouaziz, Sintering of tricalcium phosphate–fluorapatite composites with zirconia, Journal of the European Ceramic Society 28 (2008) 1995–2002.
[11] C.C. Silva, M.A. Valente, M.P.F. Graça, A.S.B. Sombra, Preparation and optical characterization of hydroxyapatite and ceramic systems with titanium and zirconium formed by dry high-energy mechanical alloying, Solid State Sciences 6 (2004) 1365–1374.
[12] Z. Evis, Reactions in hydroxylapatite–zirconia composites, Ceramics International 33 (2007) 987–991.
[13] S. Nath, R. Tripathi, B. Basu, Understanding phase stability, microstructure development and biocompatibility in calcium phosphate–titania composites, synthesized from hydroxyapatite and titanium powder mixture, Materials Science and Engineering C 29 (2009) 97–107.
[14] E. Adolfsson, N. Nygren, L. Hermansson, Decomposition mechanisms in aluminum oxide–apatite systems, Journal of the American Ceramic Society 82 (1999) 2909–2912.
[15] H.W. Kim, Y.M. Kong, Y.H. Koh, H.E. Kim, Pressureless sintering and mechanical and biological properties of fluor-hydroxyapatite composites with zirconia, Journal of the American Ceramic Society 86 (2003) 2019–2026.
[16] C.L. De Castro, B.S. Mitchell, Synthesis functionalization and surface treatment of nanoparticles, in: M.I. Baraton (Ed.), Nano-Particles from Mechanical Attrition, American Scientific Publishers, Stevenson Ranch, CA, 2002, pp. 1–14.
[17] C. Suryanarayana, Mechanical alloying and milling, Progress in Materials Science 46 (2001) 1–184.
[18] B. Nasiri–Tabrizi, A. Fahami, R. Ebrahimi–Kahrizsangi, F. Ebrahimi, Nanoparticles—new trends and developments, in: F. Ebrahimi (Ed.), New Frontiers in Mechanosynthesis: Hydroxyapatite- and Fluorapatite-Based Nanocomposite Powders, InTech, Croatia, 2012, pp. 259–297.
[19] R. Ebrahimi-Kahrizsangi, B. Nasiri-Tabrizi, A. Chami, Synthesis and characterizationof fluorapatite–titania (FAp–TiO_2) nanocomposite via mechanochemical process, Solid State Sciences 12 (2010) 1645–1651.
[20] F. Sun, F.H.S. Froes, Synthesis and characterization of mechanical-alloyed Ti_xMg alloys, Journal of Alloys and Compounds 340 (2002) 220–225.
[21] J. Qian, Y. Kang, W. Zhang, Zh. Li, Fabrication, chemical composition change and phase evolution of biomorphic hydroxyapatite, Journal of Materials Science: Materials in Medicine 19 (2008) 3373–3383.
[22] E. Landi, A. Tampieri, G. Celotti, S. Sprio, Densification behavior and mechanisms of synthetic hydroxyapatites, Journal of the European Ceramic Society 20 (2000) 2377–2387.
[23] M.H. Fathi, E. Mohammadi Zahrani, Mechanical alloying synthesis and bioactivity evaluation of nanocrystalline fluoridated hydroxyapatite, Journal of Crystal Growth 311 (2009) 1392–1403.
[24] J.P. Lafon, E. Champion, D. Bernache-Assollant, Processing of AB-type carbonated hydroxyapatite $Ca_{10-x}(PO_4)_{6-x}(CO_3)_x(OH)_{2-x-2y}(CO_3)_y$ ceramics with controlled composition, Journal of the European Ceramic Society 28 (2008) 139–147.
[25] P. Pourghahramani, E. Forssberg, Review of applied particle shape descriptors and produced particle shapes in grinding environments, Part I: Particle shape descriptors, Mineral Processing and Extractive Metallurgy Review 26 (2005) 145–166.
[26] B. Nasiri-Tabrizi, P. Honarmandi, R. Ebrahimi-Kahrizsangi, P. Honarmandi, Synthesis of nanosize single-crystal hydroxyapatite via mechanochemical method, Materials Letters 63 (2009) 543–546.
[27] R. Ebrahimi-Kahrizsangi, B. Nasiri-Tabrizi, A. Chami, Characterization of single-crystal fluorapatite nanoparticles synthesized via mechanochemical method, Particuology 9 (2011) 537–544.
[28] A. Fahami, R. Ebrahimi-Kahrizsangi, B. Nasiri-Tabrizi, Mechanochemical synthesis of hydroxyapatite/titanium nanocomposite, Solid State Sciences 13 (2011) 135–141.
[29] A. Fahami, B. Nasiri-Tabrizi, R. Ebrahimi-Kahrizsangi, Synthesis of calcium phosphate-based composite nanopowders by mechanochemical process and subsequent thermal treatment, Ceramics International 38 (2012) 6729–6738.
[30] Y.M. Sung, D.H. Kim, Crystallization characteristics of yttria-stabilized zirconia/hydroxyapatite composite nanopowder, Journal of Crystal Growth 254 (2003) 411–417.